Available online at www.sciencedirect.com
ScienceDirect
Comput. Methods Appl. Mech. Engrg. 309 (2016) 1–18
Computer methods in applied mechanics and engineering
www.elsevier.com/locate/cma

An updated Lagrangian method with error estimation and adaptive remeshing for very large deformation elasticity problems: The three-dimensional case

S. Léger*, A. Pepin

Département de mathématiques et de statistique, Pavillon Rémi-Rossignol, 18 avenue Antonine-Maillet, Université de Moncton, Moncton, Canada, E1A 3E9

Received 4 August 2015; received in revised form 26 May 2016; accepted 27 May 2016
Available online 8 June 2016

Abstract

Solving large deformation problems of hyperelastic materials by the finite element method is still a challenging problem due to the severe mesh distortion that occurs during the computation. In Leger et al. (2014), it was shown that combining an updated Lagrangian method with an efficient adaptive remeshing algorithm, an accurate transfer method for the deformation gradient tensor as well as an efficient continuation method leads to a very stable, efficient and accurate algorithm to solve two-dimensional very large deformation problems. In this paper, we show that this method can also be generalized to solve three-dimensional problems. A number of static problems will be presented and analyzed.
© 2016 Elsevier B.V. All rights reserved.

Keywords: Finite element method; Large deformations; Hyperelastic materials; Updated Lagrangian method; Adaptative remeshing; Transfer of variables

1. Introduction

Adaptive remeshing has proved to be a very efficient tool when dealing with distorted elements that appear in the mesh during the simulation of large deformation problems. The most classical approach of adaptive remeshing is based on the definition of a solution dependent metric (see [1,2]). Metric-based adaptation methods lead to good results. However, for most of these methods, an accurate estimation of the Hessian matrix of the finite element solution is needed, which is one of the difficulties of this approach. Recovering first order derivatives of a piecewise continuous finite element solution is not an easy task, and the situation is even more difficult for second order derivatives. A new approach, based on a hierarchical error indicator, was thus introduced by Bois et al. [3,4] in order to obtain a totally general adaptation method which can be applied to all sort of partial differential equation (PDE) problems and for finite element approximation of all degrees. This adaptation method leads to anisotropic meshes when the solution

* Corresponding author.
E-mail address: sophie.leger@umoncton.ca (S. Léger).

http://dx.doi.org/10.1016/j.cma.2016.05.036
0045-7825/© 2016 Elsevier B.V. All rights reserved.

allows it and has two main objectives: control the error on the solution and avoid reversed elements in regions of severe deformations.

In an updated Lagrangian context [5], remeshing intermediate configurations when distorted elements appear in the mesh is key to attaining very large deformations. A good remeshing algorithm is thus important and it was shown in [6] that the anisotropic mesh adaptation method developed by Bois et al. is a very helpful tool when mesh optimization is needed. Not only does this method lead to optimal meshes when the Hessian of the solution is indefinite, but it also improves the accuracy of the numerical results.

However, to pursue with the computation after a remeshing step, data transfer from the old mesh to the new one is required and this is a very delicate issue. If the transfer is not done properly, accuracy can be seriously affected. In an updated Lagrangian method, the deformation gradient tensor is updated at each increment in order to keep track of the previous deformations. This variable, which has its values generally known only at the Gauss points, therefore needs to be transferred to the new mesh as accurately as possible. Different techniques exist for the transfer of this variable (diffuse approximation method [7], closest point technique [8], weighted average method [9], etc.), but it was shown in [6] that the L^2-projection in a cubic field (see [10] and [11]) leads to better results, not only in terms of accuracy but also in terms of robustness.

To improve the robustness of the updated Lagrangian method, numerical continuation methods (see for example [12–15]), where the load-factor becomes an additional unknown of the system in order to control the deformation of the structure during the computation, have proved to be very powerful tools. Many continuation methods exist, but in this work, the Moore–Penrose continuation method (see [16–18]) will be considered as it has shown to be very efficient in the case of large deformation problems.

The combination of all these key ingredients (fully optimal anisotropic mesh adaptation method, cubic L^2-projection for the transfer of the deformation gradient tensor and the Moore–Penrose continuation method) led to a very stable, efficient and accurate updated Lagrangian algorithm to solve two-dimensional large deformation elasticity problems [6]. In this work, we will show that this same approach can be used to solve three-dimensional problems. The paper is organized as follows. Section 2 is devoted to the updated Lagrangian variational formulation of large deformation hyperelastic materials. Section 3 gives a brief description of the key ingredients necessary to obtain an efficient updated Lagrangian algorithm while Section 4 shows numerical examples of the overall strategy in the three-dimensional case. In this paper, we note that only static problems will be considered.

2. Theoretical developments

To describe a body undergoing large deformations using a Lagrangian framework [19], the most frequently used formulations are the total Lagrangian formulation [20], which refers to the initial configuration, and the updated Lagrangian formulation [5], which refers to the most recently calculated configuration. Both formulations are mathematically equivalent, but the updated Lagrangian formulation tends to be more appropriate when solving more complicated problems [6] (i.e. problems with strong singularities). In this work, an updated Lagrangian formulation will therefore be considered.

Let Ω^0 be the initial configuration and $\boldsymbol{X}$ the position of a material point in its configuration. The corresponding position of this point in the deformed configuration Ω^t will be denoted by $\boldsymbol{x}(\boldsymbol{X}, t)$ and the displacement field $\boldsymbol{u}$ relating $\boldsymbol{X}$ to $\boldsymbol{x}$, which are measured with respect to the same fixed rectangular Cartesian coordinate system, will be given by $\boldsymbol{u}(\boldsymbol{X}, t) = \boldsymbol{x}(\mathbf{X}, t) - \boldsymbol{X}$ (see [21] and [22]). Local deformation is measured by the deformation gradient tensor $\boldsymbol{F}$, which is defined by $\boldsymbol{F} = \frac{\partial \boldsymbol{x}}{\partial \boldsymbol{X}} = \boldsymbol{I} + \boldsymbol{\nabla}_{\boldsymbol{X}\boldsymbol{u}}$ where $\boldsymbol{\nabla}_{\boldsymbol{X}\boldsymbol{u}} = \frac{\partial \boldsymbol{u}}{\partial \boldsymbol{X}}$ is the displacement gradient. The Cauchy–Green and Green–Lagrange tensors are defined as usual by $\boldsymbol{C} = \boldsymbol{F}^\top \cdot \boldsymbol{F}$ and $\boldsymbol{E} = \frac{1}{2}(\boldsymbol{C} - \boldsymbol{I})$.

The stress tensors used to describe the internal forces acting within a deformable body are the first and second Piola–Kirchoff stress tensors, denoted respectively by $\boldsymbol{\Pi}$ and $\mathbf{S}$. These tensors are related to the Cauchy stress tensor $\boldsymbol{\sigma}$ by the relation $\boldsymbol{\Pi} = \boldsymbol{F} \cdot \boldsymbol{S} = J\boldsymbol{\sigma} \cdot \boldsymbol{F}^{-\top}$, where $J = \det \boldsymbol{F}$ is the Jacobian of the transformation from Ω^0 to Ω^t and represents the local volume change.

2.1. Hyperelastic materials

Many models exist to describe hyperelastic materials, but in this work we will consider the Mooney–Rivlin incompressible model as it is widely used in practice. For nearly incompressible hyperelastic materials, the

incompressibility can be more readily enforced within the context of the finite element formulation, which is done by adding a volumetric energy component $U(J)$ to the distortional component $\hat{\Psi}(\boldsymbol{C})$ (which is defined by a polynomial in terms of the two first invariants J_1 and J_2 of $\hat{\boldsymbol{C}} = I_3^{-1/3}\boldsymbol{C}$, where $J_1 = I_1 I_3^{-1/3}$ and $J_2 = I_2 I_3^{-2/3}$). The total strain energy function $\Psi(\boldsymbol{C})$ is therefore written as

$$\Psi(\boldsymbol{C}) = \hat{\Psi}(\boldsymbol{C}) + U(J) \tag{1}$$

where $U(J)$ can simply be chosen as $\frac{1}{2}k(J-1)^2$. We note that the penalty number k enforces the incompressibility and represents the bulk modulus. As stated in [21], the second Piola–Kirchhoff tensor for a material defined by (1) can then be obtained in the standard manner by

$$\boldsymbol{S} = 2\frac{\partial \Psi}{\partial \boldsymbol{C}} = 2\left(\frac{\partial \hat{\Psi}}{\partial J_1}\frac{\partial J_1}{\partial \boldsymbol{C}} + \frac{\partial \hat{\Psi}}{\partial J_2}\frac{\partial J_2}{\partial \boldsymbol{C}}\right) + 2k(J-1)\frac{\partial J}{\partial \boldsymbol{C}} = \boldsymbol{S}' - pJ\boldsymbol{C}^{-1}$$

with $p = -k(J-1)$.

In the case of the Mooney–Rivlin model, the total strain energy function is given by

$$\Psi = c_1(J_1 - 3) + c_2(J_2 - 3) + \frac{1}{2}k(J-1)^2$$

which leads to

$$\boldsymbol{S}' = 2c_1 I_3^{-1/3}\left(\boldsymbol{I} - \frac{1}{3}I_1\boldsymbol{C}^{-1}\right) + 2c_2 I_3^{-2/3}\left(I_1\boldsymbol{I} - \boldsymbol{C} - \frac{2}{3}I_2\boldsymbol{C}^{-1}\right). \tag{2}$$

We note that I_1, I_2 and I_3 are the invariants of $\boldsymbol{C}$ and are defined by $I_1 = \operatorname{tr}\boldsymbol{C}$, $I_2 = \frac{1}{2}\left({I_1}^2 - (\boldsymbol{C}:\boldsymbol{C})\right)$ and $I_3 = \det \boldsymbol{C} = J^2$. We also note that the fourth-order elasticity tensor $\boldsymbol{\mathcal{C}}$ is also derived from the potential energy function Ψ as $\boldsymbol{\mathcal{C}} = 4\frac{\partial^2 \Psi}{\partial \boldsymbol{C}^2}$.

2.2. Updated Lagrangian formulation

In a total Lagrangian formulation, the equilibrium equation is written in terms of the initial configuration Ω^0:

$$\begin{cases} -\nabla_{\boldsymbol{X}} \cdot \boldsymbol{\Pi} = \boldsymbol{r}_0 & \text{in } \Omega^0 \\ \boldsymbol{u} = \boldsymbol{u}_0 & \text{on } \Gamma_D^0 \\ \boldsymbol{\Pi} \cdot \boldsymbol{N} = P\,J(\boldsymbol{F}^{-\top} \cdot \boldsymbol{N}) & \text{on } \Gamma_P^0 \end{cases} \tag{3}$$

where Γ_D^0 and Γ_P^0 represent, respectively, the regions of the boundary of Ω^0 on which Dirichlet and pressure load boundary conditions are imposed. We note that $\boldsymbol{N}$ is the unit normal vector to Γ_P^0 while P represents the value of the pressure load.

The corresponding mixed variational formulation, which is a more appropriate choice in the case of incompressibility, is given by

$$\int_{\Omega^0} \boldsymbol{S}' : \left(\boldsymbol{F}^{\top} \cdot \nabla_{\boldsymbol{X}}\boldsymbol{w}\right) dV - \int_{\Omega^0} pJ\boldsymbol{F}^{-\top} : \nabla_{\boldsymbol{X}}\boldsymbol{w}\, dV = \int_{\Omega^0} \boldsymbol{r}_0 \cdot \boldsymbol{w}\, dV + \int_{\Gamma_P^0} P\boldsymbol{w} \cdot (\boldsymbol{F}^{-\top} \cdot \boldsymbol{N})J\, dA$$

$$\int_{\Omega^0} (J-1)q\, dV + \int_{\Omega^0} \frac{1}{k}pq\, dV = 0$$

where $\boldsymbol{w}$ are finite element weighting functions that vanish on Γ_D^0 and q are scalar weighting functions associated with p, where $p = -k(J-1)$ as stated above. This formulation is entirely equivalent to the incremental formulation described in [22].

In an updated Lagrangian formulation, the formulation refers to the most recently calculated configuration. By denoting the deformed configuration at the end of the ith step (which is the same as the configuration at the beginning of step $(i+1)$) by Ω^i and the coordinates in this configuration by $\boldsymbol{X}_i$, it follows that:

$$\phi_{i\to j}(\boldsymbol{X}_i) = \boldsymbol{X}_j = \boldsymbol{X}_i + \boldsymbol{u}_{i\to j}$$

$$\boldsymbol{u}_{0\to i} = \boldsymbol{u}_{0\to 1} + \boldsymbol{u}_{1\to 2} + \cdots + \boldsymbol{u}_{(i-2)\to(i-1)} + \boldsymbol{u}_{(i-1)\to i},$$
$$\phi_{0\to i} = \phi_{(i-1)\to i} \circ \phi_{(i-2)\to(i-1)} \circ \cdots \circ \phi_{1\to 2} \circ \phi_{0\to 1}$$

and

$$\boldsymbol{F}_{0\to i} = \boldsymbol{F}_{(i-1)\to i} \cdot \boldsymbol{F}_{(i-2)\to(i-1)} \cdot \ldots \cdot \boldsymbol{F}_{1\to 2} \cdot \boldsymbol{F}_{0\to 1}$$

where $\phi_{i\to j}$ is the transformation between Ω^i and Ω^j and $\boldsymbol{u}_{i\to j}$ is the displacement between the two configurations in consideration. As for the deformation gradient tensor $\boldsymbol{F}_{i\to j}$, it is defined by $(\boldsymbol{F}_{i\to j})_{mn} = \frac{\partial (\boldsymbol{X}_j)_m}{\partial (\boldsymbol{X}_i)_n}$, where $(\boldsymbol{X}_j)_m$ is the mth component of $\boldsymbol{X}_j$. The determinant of the deformation gradient tensor can therefore be expressed as:

$$J_{0\to i} = J_{(i-1)\to i} J_{(i-2)\to(i-1)} \ldots J_{1\to 2} J_{0\to 1}.$$

The updated Lagrangian formulation can be established, as shown in [6], by assuming we want to calculate the displacement between an initial configuration Ω^0 and the configuration at the end of the second step Ω^2, but by taking the intermediate configuration Ω^1 as the reference configuration for the second step. Starting from a total Lagrangian formulation expressed in terms of the notation that we have just introduced and using the fact that $\nabla_{X_i}\boldsymbol{w} = \nabla_{X_j}\boldsymbol{w} \cdot \boldsymbol{F}_{i\to j}$, it can be shown that the mixed formulation in an updated Lagrangian context is given by:

$$\begin{aligned} R_1 &= \int_{\Omega^1} \widetilde{\boldsymbol{S}}'(\boldsymbol{C}_{0\to 2}) : \left(\boldsymbol{F}_{1\to 2}^{\top} \cdot \nabla_{\boldsymbol{X_1}}\boldsymbol{w}\right) dX_1 - \int_{\Omega^1} p J_{1\to 2} \boldsymbol{F}_{1\to 2}^{-\top} : \nabla_{\boldsymbol{X_1}}\boldsymbol{w}\, dX_1 - \int_{\Omega^1} \boldsymbol{r}_1 \cdot \boldsymbol{w}\, dX_1 \\ &\quad - \int_{\Gamma_P^1} P\boldsymbol{w} \cdot (\boldsymbol{F}_{1\to 2}^{-\top} \cdot \boldsymbol{N}_1) J_{1\to 2}\, dA_1 \\ R_2 &= \int_{\Omega^1} \left(-(J_{1\to 2} - J_{0\to 1}^{-1}) - \frac{1}{k} p J_{0\to 1}^{-1}\right) q\, dX_1 \end{aligned}$$

where $\boldsymbol{r}_1 = J_{0\to 1}^{-1}\boldsymbol{r}_0$. We also note that

$$\widetilde{\boldsymbol{S}}'(\boldsymbol{C}_{0\to 2}) = J_{0\to 1}^{-1} \boldsymbol{F}_{0\to 1} \cdot \boldsymbol{S}'(\boldsymbol{C}_{0\to 2}) \cdot \boldsymbol{F}_{0\to 1}^{\top}$$

with

$$\boldsymbol{C}_{0\to 2} = \boldsymbol{F}_{0\to 1}^{\top} \cdot \boldsymbol{C}_{1\to 2} \cdot \boldsymbol{F}_{0\to 1}. \tag{4}$$

The linearized system is therefore given by:

$$\begin{aligned} \frac{\partial R_1}{\partial \boldsymbol{u}} \cdot \boldsymbol{\delta}_u - \int_{\Omega^1} \delta_p J_{1\to 2} \boldsymbol{F}_{1\to 2}^{-\top} : \nabla_{\boldsymbol{X}_1}\boldsymbol{w}\, dX_1 &= -R_1 \\ -\int_{\Omega^1} q\, J_{1\to 2} \boldsymbol{F}_{1\to 2}^{-\top} : \nabla_{\boldsymbol{X}_1}\boldsymbol{\delta}_u\, dX_1 - \int_{\Omega^1} \frac{1}{k}\delta_p q\, J_{0\to 1}^{-1}\, dX_1 &= -R_2 \end{aligned} \tag{5}$$

with

$$\begin{aligned} \frac{\partial R_1}{\partial \boldsymbol{u}} \cdot \boldsymbol{\delta}_u &= \int_{\Omega^1} \widetilde{\boldsymbol{S}}(\boldsymbol{C}_{0\to 2}) : \left(\nabla_{\boldsymbol{X}_1}^{\top}(\boldsymbol{\delta}_u) \cdot \nabla_{\boldsymbol{X_1}}\boldsymbol{w}\right) dX_1 \\ &\quad + \int_{\Omega^1} \widetilde{\boldsymbol{\mathcal{C}}}(\boldsymbol{C}_{0\to 2}) : \left(\boldsymbol{F}_{1\to 2}^{\top} \cdot \nabla_{\boldsymbol{X_1}}(\boldsymbol{\delta}_u)\right) : \left(\boldsymbol{F}_{1\to 2}^{\top} \cdot \nabla_{\boldsymbol{X_1}}\boldsymbol{w}\right) dX_1 \\ &\quad - \int_{\Gamma_P^1} P\boldsymbol{w} \cdot \left[\boldsymbol{F}_{1\to 2}^{-\top} : \nabla_{\boldsymbol{X_1}}(\boldsymbol{\delta}_u)\right] \cdot \left(\boldsymbol{F}_{1\to 2}^{-\top} \cdot \boldsymbol{N}_1\right) J_{1\to 2}\, dA_1 \\ &\quad + \int_{\Gamma_P^1} P\boldsymbol{w} \cdot \left[\left(\boldsymbol{F}_{1\to 2}^{-\top} \cdot \left(\nabla_{\boldsymbol{X_1}}\boldsymbol{\delta}_u\right)^{\top} \cdot \boldsymbol{F}_{1\to 2}^{-\top}\right) \cdot \boldsymbol{N}_1\right] J_{1\to 2}\, dA_1 \end{aligned}$$

where $\widetilde{\boldsymbol{S}}(\boldsymbol{C}_{0\to 2}) = J_{0\to 1}^{-1}\boldsymbol{F}_{0\to 1} \cdot \boldsymbol{S}(\boldsymbol{C}_{0\to 2}) \cdot \boldsymbol{F}_{0\to 1}^{\top}$. As for the tensor $\widetilde{\boldsymbol{\mathcal{C}}}(\boldsymbol{C}_{0\to 2})$, its components are given by:

$$\left(\widetilde{\boldsymbol{\mathcal{C}}}(\boldsymbol{C}_{0\to 2})\right)_{mnop} = J_{0\to 1}^{-1} \left(\boldsymbol{\mathcal{C}}(\boldsymbol{C}_{0\to 2})\right)_{ijkl} (\boldsymbol{F}_{0\to 1})_{mi} (\boldsymbol{F}_{0\to 1})_{nj} (\boldsymbol{F}_{0\to 1})_{ok} (\boldsymbol{F}_{0\to 1})_{pl}. \tag{6}$$

As can be seen, this updated Lagrangian formulation is based on the last converged state, which is different from the more classical formulation based on the current configuration as described in [22]. The two updated Lagrangian formulations are obviously mathematically equivalent to the total Lagrangian one, but the formulation presented in this work is preferred due to our error estimation and adaptation method that will be described in the next section. The algorithm used to solve large deformation problems based on this updated Lagrangian formulation can again be found in [6].

3. Key ingredients

The updated Lagrangian method used in this work will combine three key ingredients: a fully optimal anisotropic mesh adaptation method, a cubic L^2-projection for the transfer of the deformation gradient tensor and the Moore–Penrose continuation method. The following briefly describes each of these ingredients.

3.1. Mesh adaptation based on a hierarchical error indicator

The hierarchical error indicator used in this work, which was first introduced by Bois et al. [3,4], is based on the construction of a more accurate approximation of the analytic solution of our PDE problem. Let u be the analytic solution of our problem (which in our specific case will represent the unknown displacement field) and let us assume that $u_h^{(k)}$ is a finite element approximation of degree k of u. Our objective is now to estimate the error $\|u - u_h^{(k)}\|$ in some appropriate norm. The idea behind this approach is to construct a more accurate approximation $\hat{u}_h^{(k+1)}$ of degree $k+1$ of u, which can then be used to easily approximate the error by the relation

$$\|u - u_h^{(k)}\| \leq \|u - \hat{u}_h^{(k+1)}\| + \|\hat{u}_h^{(k+1)} - u_h^{(k)}\| \simeq \|\hat{u}_h^{(k+1)} - u_h^{(k)}\|. \tag{7}$$

The construction of $\hat{u}_h^{(k+1)}$ not only requires the finite element solution $u_h^{(k)}$, but also the reconstruction of a piecewise continuous Lagrange approximation of degree k of its gradient (denoted $\boldsymbol{g}_h^{(k)}$). We note that simply taking the derivative of $u_h^{(k)}$ would lead to a discontinuous approximation and it is well known that such an approximation is not very accurate. Different methods exist to obtain an accurate reconstruction of the gradient. Zienkiewicz and Zhu [23,24] were among the first to introduce such methods, but Zhang and Naga [25] introduced a more accurate method which was shown to be superconvergent on a number of finite difference meshes. This last method will therefore be used in this work to obtain an accurate approximation $\boldsymbol{g}_h^{(k)}$ of the gradient of our finite element solution.

The finite element approximation $\hat{u}_h^{(k+1)}$ is built on an element by element basis. In fact, on each element of the mesh, we look for an approximation of the form:

$$\hat{u}_h^{(k+1)} = u_h^{(k)} + c_h^{(k+1)} \tag{8}$$

where $c_h^{(k+1)}$ can be seen as a correction of degree $k+1$ of the finite element solution $u_h^{(k)}$. In the simplest case ($k = 1$), $u_h^{(1)}$ would be a piecewise linear approximation with degrees of freedom associated to the vertices of the triangle while $c_h^{(2)}$ would be a quadratic correction with degrees of freedom associated to mid-side nodes. The general definition of $c_h^{(k+1)}$ is based on the use of hierarchical Lagrange finite element basis as described in [4].

To obtain the unknown correction $c_h^{(k+1)}$, which is needed for the construction of $\hat{u}_h^{(k+1)}$, we simply use the fact that since $\hat{u}_h^{(k+1)}$ is an approximation of u and $\boldsymbol{g}_h^{(k)}$ is an approximation of its gradient ∇u, then the different partial derivatives of order $k+1$ of $\hat{u}_h^{(k+1)}$ should coincide with the appropriate partial derivative of order k of one of the components of $\boldsymbol{g}_h^{(k)}$. On each element K of the mesh, the unknown correction $c_h^{(k+1)}$ can thus be obtained by solving a small linear system and the L^2-norm of the error can be approximated by:

$$\|u - u_h^{(k)}\|_{0,K} \simeq \|\hat{u}_h^{(k+1)} - u_h^{(k)}\|_{0,K} = \|c_h^{(k+1)}\|_{0,K}.$$

The details of this procedure can again be found in [4].

With this error indicator, we can then modify the mesh in order to control the error on the finite element solution. The global strategy is to try to reach a given error level in L^2-norm throughout the domain, but we will also try

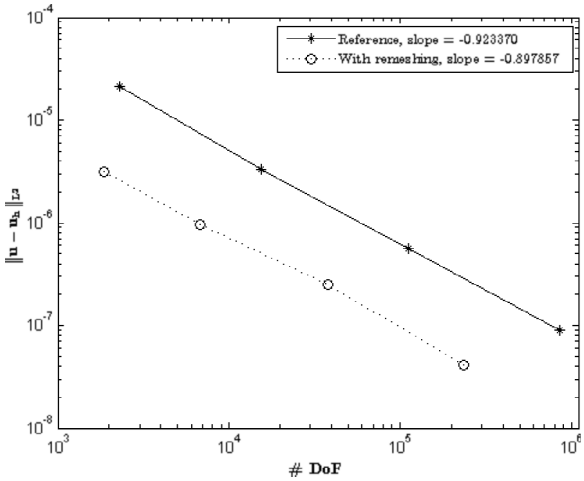

Fig. 1. Illustration of how the proposed adaptive remeshing technique improves the accuracy of the solution. Convergence curves in L^2-norm: comparison between regular and adapted meshes.

to achieve an equidistribution of the error by minimizing the H^1-seminorm of the error. To obtain the new mesh, only local operators are used. These local operators are: edge division, node elimination, edge swapping and node displacement. The first two are used to reach the given error level while the last two are used to equidistribute the error and improve the quality of the elements. These local operators also allow for anisotropic meshes where the solution allows it.

To show that this mesh adaptation method is well adapted to solve three-dimensional problems, let us use the method of manufactured solutions as described in [26,27]. For this example, the function $\boldsymbol{u} = [\ln(1 - 40X/50)/1000, \ln(1 - 40Y/50)/1000, Z/25]$ will be chosen as the analytical solution of the total displacement, where X, Y and Z are the coordinates on $\Omega^0 = [0, 1]^3$. We will solve using the updated Lagrangian method described in Section 2.2 and use $k = 100$, $c_1 = 1$ and $c_2 = 2$ as parameters for the Mooney–Rivlin model. A Dirichlet boundary condition of $\boldsymbol{u} = [\ln(1 - 40X/50)/5000, \ln(1 - 40Y/50)/5000, Z/125]$ will be imposed on all the mesh boundaries for each of the five updated Lagrangian steps and P_2–P_1 elements (quadratic discretization for the displacement and linear for the pressure also known as the Taylor–Hood element [28]) will be used to generate the convergence curves. The reference curve will be obtained without remeshing and will be compared with the convergence curve obtained when using the proposed adaptive remeshing method on the initial configuration.

Fig. 1 clearly shows that for a given number of degrees of freedom (DoFs), the error is lower in the case of our proposed adaptive remeshing technique. We can also see that the mesh adaptation maintains an optimal convergence rate. The hierarchical mesh adaptation method was also compared with a metric based adaptation method (see [1,29]) and the results are shown in Fig. 2. As can be seen, the proposed hierarchical adaptive remeshing technique leads to more accurate results, which is another reason why this method is preferred.

3.2. Data transfer

One of the most important variable to transfer from the old mesh to the new one in an updated Lagrangian context is the deformation gradient tensor, denoted as $\boldsymbol{F}_{0\to1}$ in our algorithm, as it is needed to keep track of the previous deformations. This variable is known only at the Gauss points of the actual mesh and needs to be transferred to the Gauss points of the new mesh as accurately as possible. In [6], we considered three different techniques to achieve this goal: closest point technique (see [8]), weighted average method with different weight functions (see [9]) and the L^2-projection method (see [10] and [11]) in different degree fields (i.e. L^2-projection in linear, quadratic and cubic field). Amongst the methods studied, the L^2-projection in a cubic field not only led to the most accurate results, but also proved to be the most robust. The L^2-projection method consists of the following four steps :

1. Extrapolate the variable from the Gauss points to the nodes of the old mesh by the least-squares method.
2. Locate the nodes of the new mesh with respect to the local coordinate systems of the elements of the old mesh.

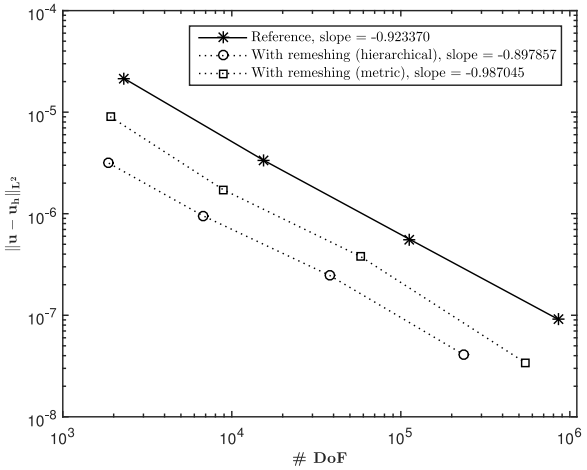

Fig. 2. Convergence curves in L^2-norm: comparison between our hierarchical mesh adaptation method and a metric based adaptation method.

3. Calculate the value of the variable at the nodes of the new mesh by direct interpolation.
4. Obtain the values of the variable at the Gauss points of the new mesh by employing the shape functions of the new mesh.

In step 1, the least-squares method can be applied globally on the entire domain Ω [30–32], locally on a patch of elements [23,33,34] or even locally element-wise [30]. In this work, we will again study the effect of using different order smoothing shape functions in the global least-squares method to solve large deformation hyperelastic problems, but this time in the three-dimensional case.

Let Z^* denote a variable with its values only known at the Gauss points. In the global case, the projection method requires solving the following minimization problem

$$\min_{Z \in V_h^k} \frac{1}{2} \int_\Omega (Z - Z^*)^2 \, d\Omega \quad \Leftrightarrow \quad \int_\Omega Z \, q \, d\Omega = \int_\Omega Z^* \, q \, d\Omega, \quad \forall q \in V_h^k \tag{9}$$

where V_h^k is the finite element space of continuous piecewise polynomials of degree k and Ω is the configuration of the old mesh (of the last converged state). This is equivalent to an L^2-projection of Z^* onto the finite element function space V_h^k where q are the test functions in V_h^k.

We note that the computational cost of this projection step is minimal even in the three-dimensional case as the resolution of the corresponding linear systems is done by a preconditioned conjugate gradient method. Also, we note that in the specific case of the deformation gradient tensor, this projection is performed component wise noticing that the global (mass) matrix is the same for all components.

To show that the L^2-projection method in a cubic field also leads to the best results in the three-dimensional case, let us consider three different test problems.

3.2.1. Horizontal elastic beam problem

Let us first consider an horizontal beam of dimension $10 \times 1 \times 1$ fixed at its left side on which we will apply a total pressure load of $P = 0.003$ on the top edge. The pressure will be applied gradually during three updated Lagrangian steps of 0.001, and then released gradually during the following three steps. At the end of the sixth step, the forces will no longer be applied and the beam should return to its original configuration. The total displacement should therefore be null. However, since adaptive remeshing will be completed at the end of each step, which means that the deformation gradient tensor will be transferred a total of five times (no remeshing will be done at the end of the sixth step), the best we can hope for is a good approximation of the initial configuration. Our goal will therefore be to find the transfer method that minimizes the total displacement. We note that the initial configuration will be remeshed in order to take into consideration, from the beginning, the various transitions in the solution and to improve the accuracy of the transfers of the deformation gradient tensor in subsequent remeshing steps. Remeshing the initial configuration does not necessitate any transfer of variables, which means that no loss of information will result from this.

Table 1
Horizontal elastic beam problem: L^2-norm of the total displacement after unloading divided by the volume of the initial geometry (comparison of the different transfer techniques).

L^2-projection $k = 1$	L^2-projection $k = 2$	L^2-projection $k = 3$	CPT	WAM $(1/d^4)$
4.194×10^{-3}	3.360×10^{-4}	7.500×10^{-5}	3.697×10^{-3}	3.460×10^{-3}

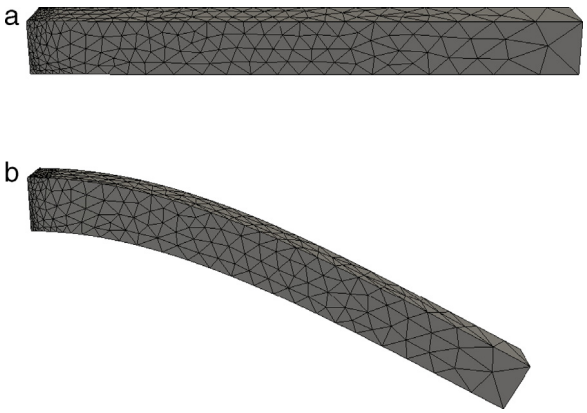

Fig. 3. (a) Initial adapted mesh. (b) Deformed mesh at $P = 0.003$.

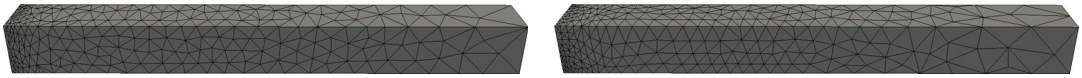

(a) Hierarchical remeshing. (b) Metric based remeshing.

Fig. 4. Horizontal elastic beam problem: initial meshes for both remeshing methods.

Fig. 3 shows the adapted mesh of the initial geometry, which has 5447 nodes and 3233 elements, as well as the deformed mesh after the third step (at $P = 0.003$) in the case of a cubic L^2-projection. We note that P_2–P_1 elements were used for the computation and that the parameters for the Mooney–Rivlin model were chosen as $k = 100$, $c_1 = 1.5$ and $c_2 = 0.5$. We also note that the Taylor–Hood element satisfies the inf–sup condition (also known as the Babuska–Brezzi condition) and can therefore be used in the case of incompressible materials (see [28] and [35]).

Table 1 compares the L^2-projection method in different degree fields (linear, quadratic and cubic) with the closest point technique (CPT) and the weighted average method (WAM) with weight functions $1/d^4$ by giving the normalized L^2-norm of the total displacement for each of the methods. As can be seen, the cubic L^2-projection is approximately fifty times better than the linear L^2-projection, the closest point technique and the weighted average method, and approximately four times better than the quadratic L^2-projection. This test clearly illustrates the better performance of the cubic L^2-projection and justifies why this method is used in our complete updated Lagrangian method.

A similar test was also done to compare the difference in accuracy when using our proposed hierarchical adaptive remeshing technique versus a metric based remeshing algorithm in the case of a cubic L^2-projection method. For this test, a total pressure load of $P = 0.002$ was applied in the first updated Lagrangian step and was released during the second step. After the first step (at $P = 0.002$), the configuration was remeshed and the deformation gradient tensor was transferred (using a cubic L^2-projection). We note that, in both cases, the initial configuration was also remeshed. Table 2 compares the normalized L^2-norm of the total displacement for each of the remeshing methods and shows that the hierarchical adaptive remeshing method leads to more accurate results even when the transfer of the deformation gradient tensor is necessary (and even for a mesh with a slightly lower number of DoFs). Fig. 4 compares the initial meshes for both remeshing methods.

Table 2
Horizontal elastic beam problem: L^2-norm of the total displacement after unloading divided by the volume of the initial geometry (comparison of the different remeshing techniques).

	# DoFs	Error
Metric based remeshing	20 198	2.060×10^{-4}
Hierarchical remeshing	18 659	1.440×10^{-4}

Table 3
Indentation problem with pressure load: L^2-norm of the total displacement after unloading divided by the volume of the initial geometry (comparison of the different transfer techniques).

L^2-projection $k = 1$	L^2-projection $k = 2$	L^2-projection $k = 3$	CPT	WAM $(1/d^4)$
3.305×10^{-5}	1.188×10^{-5}	4.855×10^{-6}	3.700×10^{-5}	1.455×10^{-4}

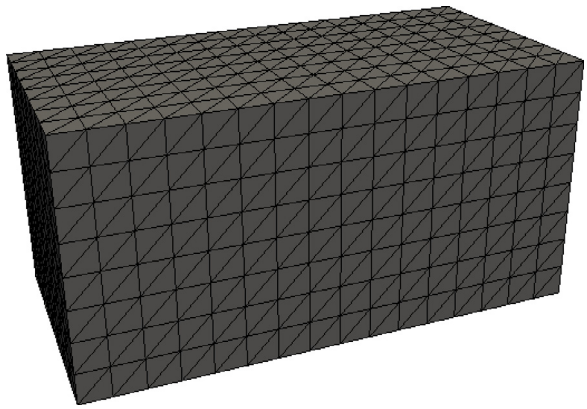

Fig. 5. Indentation problem with pressure load: uniform initial mesh.

3.2.2. *Indentation problem with pressure load*

The previous example demonstrated that the cubic L^2-projection method works well in the case of homogeneous deformations. To show that it also works well when dealing with more difficult problems, let us consider a rectangular prism of dimension $2 \times 1 \times 1$ on which a total pressure load of $P = 6$ will be applied on the left part of the top edge (see Fig. 5). The two different types of boundary conditions on the top edge will lead to a strong singularity at the interface, leading to a more difficult problem to solve than the horizontal elastic beam problem. The pressure will be applied gradually during six updated Lagrangian steps of $\Delta P = 1$, and then released gradually during the following six steps. Theoretically, the total displacement should again be null. The initial configuration will be remeshed to take into consideration the various transitions in the solution from the start and subsequent remeshing steps will be done at every three updated Lagrangian steps. A total of five remeshing steps will therefore be done during the simulation (including the initial remeshing).

Fig. 6 shows the deformed mesh after the sixth step (at $P = 6$) in the case of a cubic L^2-projection. We note that P_2–P_1 elements were again used for the computation and that the parameters for the Mooney–Rivlin model were chosen as $k = 1000$, $c_1 = 1.5$ and $c_2 = 0.5$. Table 3 compares the different transfer techniques and again illustrates the better performance of the cubic L^2-projection.

A more challenging problem would now be to consider a heterogeneous problem with a strong material discontinuity. Many authors have studied the effect of error estimation on these types of problems. We refer the reader to [36–38] for discussions on this topic.

To test the performance of the cubic L^2-projection as well as our mesh adaptation method in such a situation, let us consider again the prism of Fig. 5, but this time, where a prism of dimension $0.5 \times 0.25 \times 0.25$ will be completely

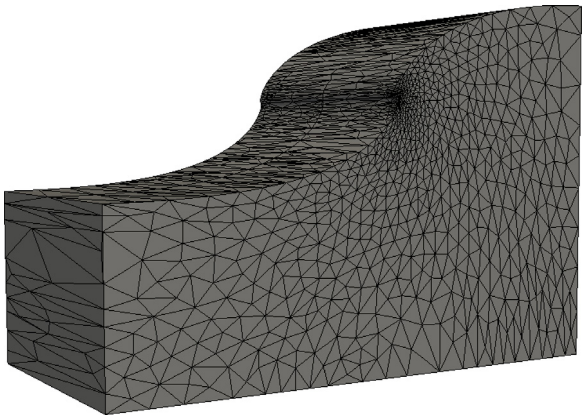

Fig. 6. Indentation problem with pressure load: deformed configuration after the sixth step ($P = 6$).

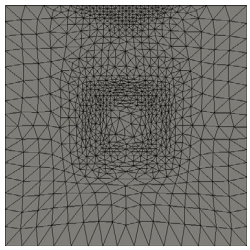

Fig. 7. 2D heterogeneous problem with a strong material discontinuity: initial adapted mesh.

Table 4
Heterogeneous problem in 2D: L^2-norm of the total displacement after unloading divided by the area of the initial geometry (comparison of the different transfer techniques).

L^2-projection $k = 1$	L^2-projection $k = 2$	L^2-projection $k = 3$	CPT	WAM $(1/d^4)$
2.104×10^{-4}	4.374×10^{-5}	1.008×10^{-5}	1.035×10^{-4}	9.701×10^{-5}

immersed inside the other prism. The inner prism will consist of a stiff region which will be represented by higher values of parameters in the Mooney–Rivlin model: $k = 1000$, $c_1 = 15$ and $c_2 = 5$. P_2–P_1 elements will again be used for the computation and a pressure load will be applied on the left part of the top edge following the same procedure as in the previous example.

To better understand the difficulty of this problem and to better illustrate the effect of remeshing on these types of problems, let us first consider the two-dimensional case where a square of dimension 1×1 is completely immersed inside a square of dimension 4×4. Fig. 7 shows the adapted mesh on the initial geometry and illustrates how the remeshing procedure has detected the material discontinuity and how it has added elements in these regions in order to improve the accuracy of the solution. Fig. 8(a) shows the deformed configuration at $P = 6$ in the case of a cubic L^2-projection, while Fig. 8(b) shows the configuration once the load has been completely released. As can be seen in Table 4, even in the case of a more challenging problem, the cubic L^2-projection still leads to the better results (it is approximately four times better than the L^2-projection in a quadratic field, ten times better than the weighted average method and closest point technique and twenty times better than the L^2-projection in a linear field). Our mesh adaptation method also performs very well.

The same comparisons were made in the three-dimensional case, and once again, the L^2-projection in a cubic field led to the most accurate result. The results can be seen in Table 5.

To consider an even more challenging problem, let us now consider the case where a much thinner stiff reinforcement is immersed inside the soft region, which will lead to an even stronger material discontinuity. In the

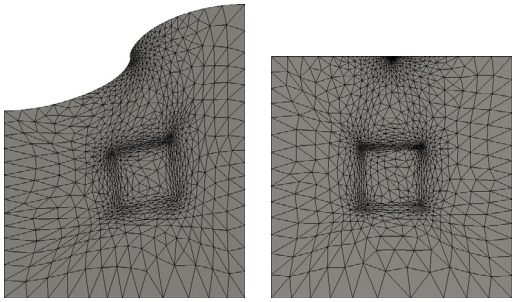

(a) Deformed configuration at $P = 6$.

(b) Configuration after releasing the load.

Fig. 8. 2D heterogeneous problem with a strong material discontinuity: evolution of the configuration.

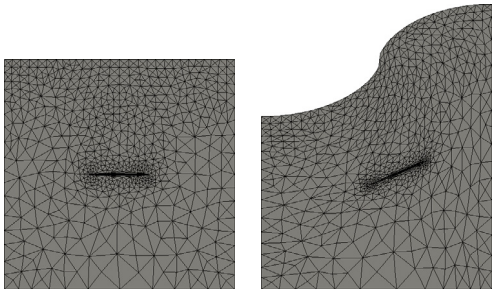

(a) Initial adapted mesh.

(b) Deformed configuration at $P = 6$.

Fig. 9. 2D heterogeneous problem with a thinner stiff reinforcement: evolution of the configuration.

Table 5
Heterogeneous problem in 3D: L^2-norm of the total displacement after unloading divided by the volume of the initial geometry (comparison of the different transfer techniques).

L^2-projection $k = 1$	L^2-projection $k = 2$	L^2-projection $k = 3$	CPT	WAM $(1/d^4)$
8.052×10^{-5}	2.054×10^{-5}	1.234×10^{-5}	5.577×10^{-5}	6.485×10^{-5}

Table 6
Heterogeneous problem in 2D with a thinner stiff reinforcement: L^2-norm of the total displacement after unloading divided by the area of the initial geometry (comparison of the different transfer techniques).

L^2-projection $k = 1$	L^2-projection $k = 2$	L^2-projection $k = 3$	CPT	WAM $(1/d^4)$
1.485×10^{-4}	4.818×10^{-5}	2.480×10^{-5}	1.083×10^{-4}	8.627×10^{-5}

two-dimensional case, a rectangle of dimension 1×0.01 will therefore be completely immersed inside a square of dimension 4×4 and the inner stiff region will be represented by even higher values of parameters in the Mooney–Rivlin model: $k = 1000$, $c_1 = 750$ and $c_2 = 250$. Fig. 9(a) shows the adapted mesh on the initial geometry and shows again how the remeshing procedure has added elements near the material discontinuity, while Fig. 9(b) shows the deformed configuration at $P = 6$ in the case of a cubic L^2-projection. As can be seen in Table 6, the cubic L^2-projection still leads to the better results in this very challenging heterogeneous problem. We note that very similar results were obtained in the three-dimensional case.

Table 7
Large rotation problem: L^2-norm of the error on p and $\boldsymbol{\sigma}$ (comparison of the different transfer techniques).

	L^2-projection $k = 1$	L^2-projection $k = 2$	L^2-projection $k = 3$	CPT	WAM $(1/d^4)$
p	3.779×10^{-2}	1.416×10^{-3}	3.614×10^{-4}	3.825×10^{-3}	1.820×10^{-2}
$\boldsymbol{\sigma}$	6.560×10^{-2}	2.490×10^{-3}	8.808×10^{-4}	6.757×10^{-2}	4.044×10^{-2}
$\boldsymbol{\sigma}$ (%)	1.13%	0.04%	0.02%	1.16%	0.69%

3.2.3. Large rotation problem

To test the efficiency of our proposed approach in the case of large rotation, let us use the method of manufactured solutions and consider the following transformation:

$$x = X\cos(\beta Z) - Y\sin(\beta Z)$$
$$y = X\sin(\beta Z) + Y\cos(\beta Z)$$
$$z = Z$$

where X, Y and Z are the coordinates on the initial configuration Ω^0 and x, y and z are the coordinates on the deformed configuration Ω^t. The solution $\boldsymbol{u}$ is therefore given by $\boldsymbol{u} = [X\cos(\beta Z) - Y\sin(\beta Z) - X, X\sin(\beta Z) + Y\cos(\beta Z) - Y, 0]$. As analytic expressions are known for the pressure p (which is defined as $p = -k(J-1)$) and the Cauchy stress tensor $\boldsymbol{\sigma}$, the error on each of these quantities will be calculated on Ω^t at the end of the simulation (since they are defined on that configuration). Evidently, analytic expressions are also known for the displacement $\boldsymbol{u}$ and the deformation gradient tensor $\boldsymbol{F}$. However, since these quantities are defined on Ω^0, the displacement would need to be subtracted from the coordinates in the current configuration to obtain the coordinates in the initial configuration before computing the L^2-norms. As remeshing is done a few times during the simulation, this would not lead to the exact initial configuration and the comparisons would not be accurate. The comparisons will therefore only be done on p and $\boldsymbol{\sigma}$.

For this comparison, β will be chosen as $\frac{\pi}{4}$ and a Mooney–Rivlin model with parameters $k = 100$, $c_1 = 1$ and $c_2 = 2$ will be used on a cube of dimension $1 \times 1 \times 1$. The simulation will be completed in four updated Lagrangian steps and remeshing will be done on the initial configuration as well as after each of the updated Lagrangian steps. Table 7 compares the errors for the different transfer methods. As can be seen, the L^2-projection in a cubic field performs, again, much better than the other transfer methods. The table also shows the relative error in L^2-norm for the Cauchy stress tensor in order to illustrate the magnitude of the errors. We note that the relative error was not calculated for the pressure as the true value is zero.

3.3. Moore–Penrose continuation method

Numerical continuation methods are very powerful and efficient tools when it comes to solving nonlinear systems of equations. They have increased in popularity during the years and have provided important contributions toward the numerical solution of highly nonlinear problems which are hard to obtain otherwise. Predictor–corrector continuation methods are the most frequently used in practice. In this work, the Moore–Penrose continuation method will be used to improve the robustness of our updated Lagrangian algorithm. This method, which introduces a load parameter λ to control the deformation of the structure during the computation, can be described as follows.

In the general case, the system of nonlinear equations to solve can be written implicitly as

$$F(x) = 0 \tag{10}$$

with $F : \mathbb{R}^{N+1} \to \mathbb{R}^N$ a smooth function. The vector of unknowns x consists of the N degrees of freedom plus the loading parameter λ.

Assuming a point $x^{(i)} \in \mathbb{R}^{N+1}$ on the solution curve $F(x) = 0$ has been found, the first step consists of calculating a tangent vector $v^{(i)} \in \mathbb{R}^{N+1}$ at this point satisfying the property

$$F_x(x^{(i)})v^{(i)} = 0. \tag{11}$$

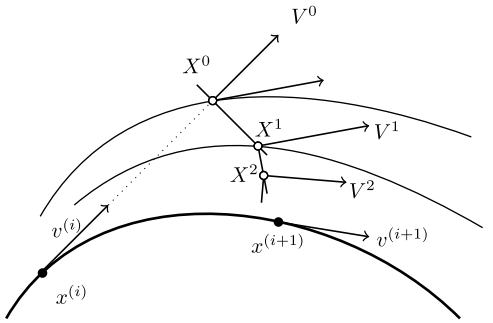

Fig. 10. Correction algorithm for the Moore–Penrose continuation method.

The tangent vector is then used to calculate the next point $x^{(i+1)} \in \mathbb{R}^{N+1}$ on the solution curve. We begin by completing a prediction step in the tangent direction:

$$X^0 = x^{(i)} + h_i v^{(i)} \tag{12}$$

and then a correction is made by searching the point $x^{(i+1)}$ solution of the system:

$$\begin{cases} F(x) = 0 \\ v^\top (x - X^0) = 0 \end{cases}$$

where $v \in \mathbb{R}^{N+1}$ satisfies $F_x(x)v = 0$. We note that the step size in the tangent direction, h_i, can be controlled based on the number of iterations to convergence or can even be determined by a line search algorithm.

By linearizing the system around X^0 and exploiting the Moore–Penrose pseudoinverse A^+ of a matrix A, the quasi-Newton iterations (also called Moore–Penrose corrections) are given by

$$X^{k+1} = X^k - F_x^+(X^k)F(X^k), \quad k = 0, 1, 2, \ldots \tag{13}$$

where $V^k \in \mathbb{R}^{N+1}$ satisfies the relation $F_x(X^k)V^k = 0$. Since V^k is unknown, it is approximated by a vector V^k satisfying

$$F_x(X^{k-1})V^k = 0, \qquad V^0 = v^{(i)}. \tag{14}$$

The numerical algorithm for the Moore–Penrose method can be found in [17]. The correction algorithm is illustrated in Fig. 10.

4. Numerical results

This section will show how our complete updated Lagrangian method, which combines error estimation, adaptive remeshing, the cubic L^2-projection transfer method for the transfer of the deformation gradient tensor and the Moore–Penrose continuation algorithm, can solve efficiently three-dimensional large deformation elasticity problems. In Section 3.2, we have shown that the cubic L^2-projection transfer method leads to the most accurate results. In this section, we will show that, by including it in our complete updated Lagrangian method, it also enables us to reach high levels of deformations.

4.1. Horizontal elastic beam

As a first example, let us consider the rectangular elastic beam of dimension $10 \times 1 \times 1$ of Fig. 11(a) on which we will apply a pressure load P on the top edge. The beam will be fixed at both extremities and the applied force will be controlled by the Moore–Penrose continuation algorithm. We note that remeshing steps will be completed when necessary (i.e. when convergence problems appear) in order to attain a sufficiently high level of deformation.

As usual, the initial configuration will be remeshed in order to take into consideration the different variations of the solution from the start. Using $P_2 - P_1$ elements and $k = 100$, $c_1 = 1.5$ and $c_2 = 0.5$ as parameters for the

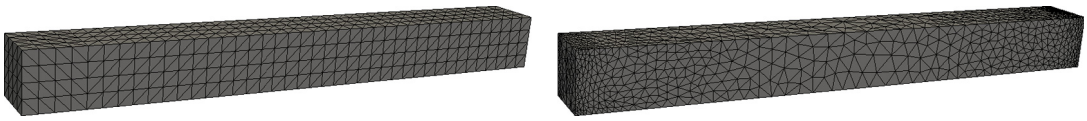

(a) Before initial remeshing. (b) After initial remeshing.

Fig. 11. Horizontal elastic beam: initial configuration.

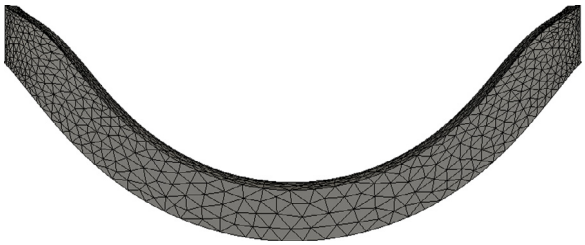

Fig. 12. Horizontal elastic beam: final deformed configuration ($P = 0.47$).

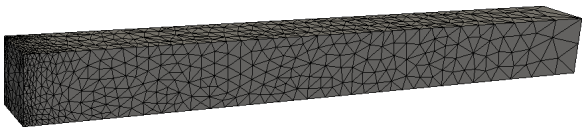

Fig. 13. Horizontal elastic beam in the case of one fixed extremity: initial adapted mesh.

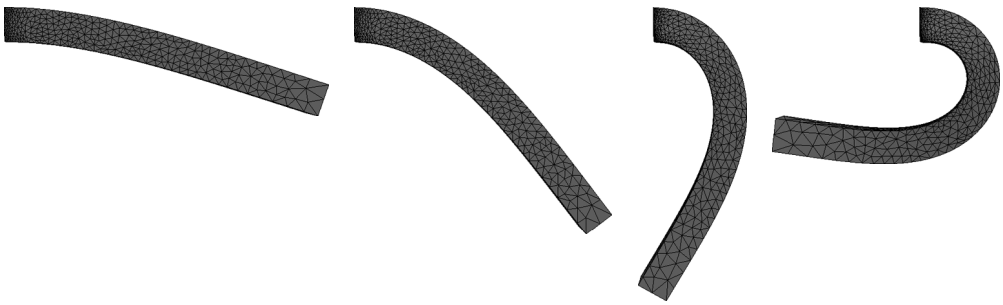

(a) $P = 0.002$. (b) $P = 0.006$. (c) $P = 0.014$. (d) $P = 0.027$.

Fig. 14. Horizontal elastic beam in the case of one fixed extremity: evolution of the deformation.

Mooney–Rivlin model, the initial remeshing step produces the mesh illustrated in Fig. 11(b), which has 24,566 nodes and 15,932 elements. As can be seen, the elements in the mesh are concentrated near both extremities of the beam, where it is fixed and where large changes appear in the solution gradient. This initial mesh is then used by our complete updated Lagrangian method. Fig. 12 illustrates the final deformed configuration of the simulation where a total load of $P = 0.47$ has been applied (corresponding to a maximum principal stretch of approximately 21.2). Considering that this is an extremely difficult problem to solve due to the strong singularities that appear at both ends of the beam, the level of deformation attained is very high.

A similar test can also be done by only fixing one of the extremities. In this case, the remeshing algorithm produces the initial mesh of Fig. 13, where this time the majority of the elements are concentrated near the left side (i.e. near the extremity that is fixed). By applying a pressure load P on the top edge of the beam (as in the first example) and by remeshing when necessary, a very high level of deformation, corresponding to a maximum principal stretch of approximately 10.1, can be attained. Fig. 14 illustrates the evolution of the beam during the simulation and confirms the last statement.

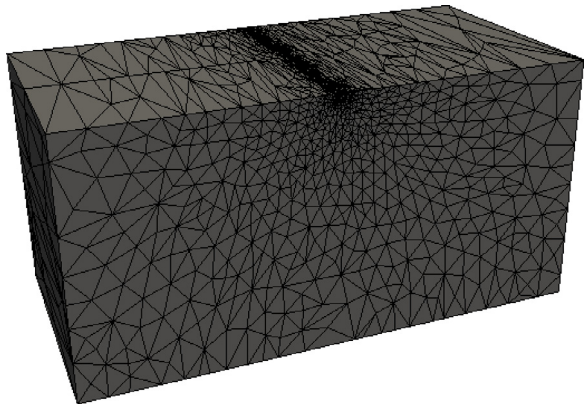

Fig. 15. Indentation problem with pressure load: adapted initial mesh.

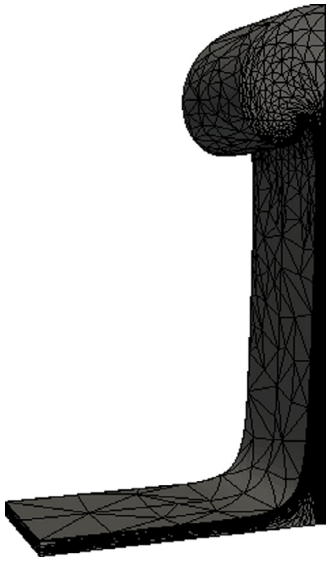

Fig. 16. Indentation problem with pressure load: final deformed mesh ($P = 202.57$).

4.2. Indentation problem with pressure load

Let us now consider the rectangular prism of Fig. 5 on which a pressure load P will again be applied on the left part of the top edge. Fig. 15 shows the adapted initial mesh (which will be used for the simulation). As can be seen, many elements have been added in the transition zone separating the two different types of limit conditions (pressure load on left and Neumann on right).

Using $P_2 - P_1$ elements and the values $k = 100$, $c_1 = 1.5$ and $c_2 = 0.5$ for the Mooney–Rivlin model, we are able to attain very large deformations (maximum principal stretch of approximately 232.3). Fig. 16 shows the final deformed configuration where a total pressure load of $P = 202.57$ has been applied.

To complexify this problem, we can consider the same initial configuration, but where this time the top edge will be divided into three parts in order to apply the pressure load on the middle part. Two transition zones of limit conditions will therefore be created on the top edge, which will lead to a much more difficult problem to solve. The key to attaining very large deformations in this example is to remesh the initial configuration in order to detect the singular regions from the start. Fig. 17 illustrates the adapted initial mesh and shows that the remeshing algorithm detects both transition zones and concentrates the majority of the elements in these regions in order to better capture the solution.

By controlling the deformation with the Moore–Penrose continuation algorithm and by remeshing the configuration twice during the simulation, we are able to achieve a total pressure load of $P = 199.64$ (which leads to a maximum

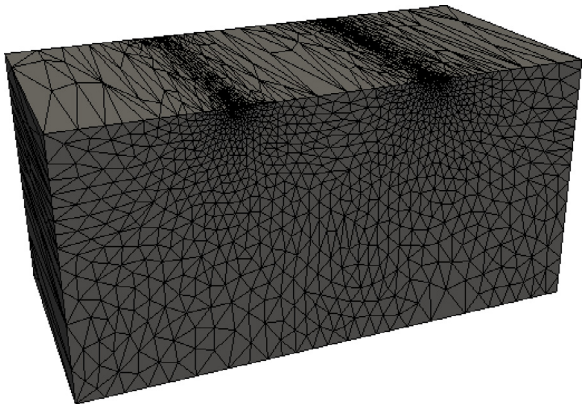

Fig. 17. Indentation problem with pressure load on the middle part of the top edge: adapted initial mesh.

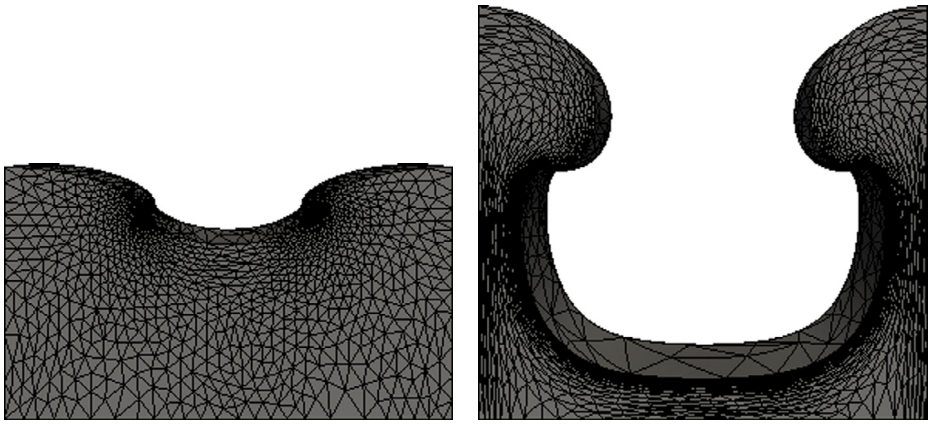

(a) $P = 7.91$.

(b) $P = 64.21$.

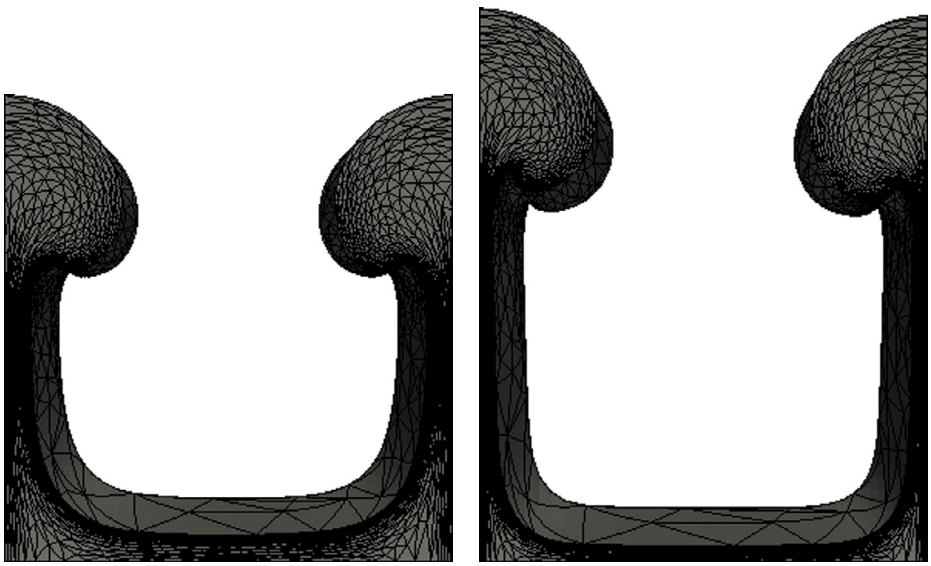

(c) $P = 101.17$.

(d) $P = 199.64$.

Fig. 18. Indentation problem with pressure load on the middle part of the top edge: evolution of the deformation.

principal stretch of approximately 171.2). Fig. 18 illustrates the evolution of the mesh during the simulation as well as the final deformed configuration.

5. Conclusion

In this work, we have presented a complete updated Lagrangian algorithm to solve three-dimensional large deformation elasticity problems. This algorithm is a generalization of the algorithm presented in [6] and includes key ingredients for its good performance, such as error estimation and adaptive remeshing, an accurate transfer method for the deformation gradient tensor as well as an efficient continuation method. Our adaptive remeshing not only leads to optimal meshes when the Hessian of the solution is indefinite, but also improves the accuracy of the numerical results. The numerical examples presented in this paper not only show the good accuracy of this method, but also its robustness in the case of complex large deformation problems. In practical applications, where accuracy and robustness is of utmost importance, this complete method has been very performant and has lead to better results. We also note that remeshing the initial configuration, which does not necessitate any transfer of variables (meaning that no loss of information results from this), has also shown to enhance the performance of the updated Lagrangian method.

Acknowledgments

The authors wish to acknowledge the financial support of the Faculty of Science of the Université de Moncton and the New Brunswick Innovation Foundation [grant number 222532].

References

[1] M. Hecht, B. Mohammadi, Mesh adaptation by metric control for multi-scale phenomena and turbulence, in: 35th Aerospace Sciences Meeting & Exhibit, number 97–0859, Reno, USA, 1997.
[2] F. Alauzet, High-order methods and mesh adaptation for Euler equations, Internat. J. Numer. Methods Fluids 56 (8) (2008) 1069–1076.
[3] R. Bois, M. Fortin, A. Fortin, A fully optimal anisotropic mesh adaptation method based on a hierarchical error estimator, Comput. Methods Appl. Mech. Engrg. 209–212 (2012) 12–27.
[4] R. Bois, M. Fortin, A. Fortin, A. Couët, High order optimal anisotropic mesh adaptation using hierarchical elements, Eur. J. Comput. Mech. 21 (1–2) (2012) 72–91, 8.
[5] K.-J. Bathe, E. Ramm, E.L. Wilson, Finite element formulations for large deformation dynamic analysis, Internat. J. Numer. Methods Engrg. 9 (2) (1975) 353–386.
[6] S. Léger, A. Fortin, C. Tibirna, M. Fortin, An updated Lagrangian method with error estimation and adaptive remeshing for very large deformation elasticity problems, Internat. J. Numer. Methods Engrg. 100 (13) (2014) 1006–1030.
[7] V. Hamel, J.M. Roelandt, J.N. Gacel, F. Schmit, Finite element modeling of clinch forming with automatic remeshing, Comput. & Struct. 77 (2) (2000) 185–200.
[8] J.F. Molinari, M. Ortiz, Three-dimensional adaptive meshing by subdivision and edge-collapse in finite-deformation dynamic-plasticity problems with application to adiabatic shear banding, Internat. J. Numer. Methods Engrg. 53 (2002) 1101–1126.
[9] AM. Habraken, S. Cescotto, A automatic remeshing technique for finite element simulation of forming processes, Internat. J. Numer. Methods Engrg. 30 (1990) 1503–1525.
[10] N.-S. Lee, K.-J. Bathe, Error indicators and adaptive remeshing in large deformation finite element analysis, Finite Elem. Anal. Des. 16 (2) (1994) 99–139.
[11] D. Perić, Ch. Hochard, M. Dutko, D.R.J. Owen, Transfer operators for evolving meshes in small strain elasto-plasticity, Comput. Methods Appl. Mech. Engrg. 137 (3–4) (1996) 331–344.
[12] E. Riks, The application of Newton's method to the problem of elastic stability, J. Appl. Mech. 39 (1972) 1060–1066.
[13] M.A. Crisfield, A fast incremental/iterative solution procedure that handles snap through, Comput Struct. 13 (1981) 55–62.
[14] K.H. Schweizerhof, P. Wriggers, Consistent linearization for path following methods in nonlinear fe analysis, Comput. Methods Appl. Mech. Engrg. 59 (1986) 261–279.
[15] J.C. Simo, P. Wriggers, K.H. Schweizerhof, R.L. Taylor, Post-buckling analysis involving inelasticity and unilateral constraints, Internat. J. Numer. Methods Engrg. 23 (1986) 779–800.
[16] E.L. Allgower, K. Georg, An Introduction to Numerical Continuation Methods, in: Springer Series in Computational Mathematics, vol. 13, Springer-Verlag, New York, 1990.
[17] A. Dhooge, W. Govaerts, Y.A. Kuznetsov, MATCONT: a MATLAB package for numerical bifurcation analysis of ODEs, ACM Trans. Math. Software 29 (2) (2003).
[18] P. Deuflhard, G. Heindl, Affine invariant convergence theorems for Newton's method and extensions to related methods, SIAM J. Numer. Anal. 16 (1) (1979) 1–10.
[19] P.G. Ciarlet, Basic error estimates for elliptic problems, in: Handbook of Numerical Analysis, vol. 2, North Holland, Amsterdam, 1991, pp. 17–351.

[20] H.D. Hibbitt, P.V. Marcal, J.R. Rice, A finite element formulation for problems of large strain and large displacement, Int. J. Solids Struct. 6 (8) (1970) 1069–1086.
[21] J. Bonet, R.D. Wood, Nonlinear Continuum Mechanics for Finite Element Analysis, Cambridge University Press, Cambridge (UK), New York, 2008.
[22] K.J. Bathe, Finite Element Procedures, Prentice-Hall, New Jersey, 1996.
[23] O.C. Zienkiewicz, J.Z. Zhu, The superconvergent patch recovery and a posteriori error estimate, Part I: The recovery technique, Internat. J. Numer. Methods Engrg. 33 (1992) 1331–1364.
[24] O.C. Zienkiewicz, J.Z. Zhu, The superconvergent patch recovery and a posteriori error estimate, Part II: Error estimates and adaptivity, Internat. J. Numer. Methods Engrg. 33 (1992) 1365–1382.
[25] Z. Zhang, A. Naga, A new finite element gradient recovery method: Superconvergence property, SIAM J. Sci. Comput. 26 (4) (2005) 1192–1213.
[26] R.C. Batra, X.Q. Liang, Finite dynamic deformations of smart structures, Comput. Mech. 20 (1997) 427–438.
[27] É. Chamberland, A. Fortin, M. Fortin, Comparison of the performance of some finite element discretizations for large deformation elasticity problems, Comput. Struct. 88 (11–12) (2010) 664–673.
[28] F. Brezzi, M. Fortin, Mixed and Hybrid Finite Element Methods, in: Springer Series in Computational Mathematics, vol. 15, Springer-Verlag, New York, 1991.
[29] F. Alauzet, P. Frey, Estimateur d'erreur géométrique et métriques anisotropes pour l'adaptation de maillage. Partie I: aspects théoriques. Technical Report 4759, INRIA, 2003.
[30] E. Hinton, J.S. Campbell, Local and global smoothing of discontinuous finite element functions using a least squares method, Internat. J. Numer. Methods Engrg. 8 (1974) 461–480.
[31] M.L. Alves, J.L.M. Fernandes, J.M.C. Rodrigues, P.A.F. Martins, Finite element remeshing in metal forming using hexahedral elements, J. Mater. Process. Technol. 141 (2003) 395–403.
[32] J.L.M. Fernandes, P.A.F. Martins, All-hexahedral remeshing for the finite element analysis of metal forming processes, Finite Elem. Anal. Des. 43 (2007) 666–679.
[33] A.R. Khoei, S.A. Gharehbaghi, A.R. Tabarraie, A. Riahi, Error estimation, adaptivity and data transfer in enriched plasticity continua to analysis of shear band localization, Appl. Math. Model. 31 (2007) 983–1000.
[34] A.R. Khoei, S.A. Gharehbaghi, Three-dimensional data transfer operators in large plasticity deformations using modified-SPR technique, Appl. Math. Model. 33 (2009) 3269–3285.
[35] D. Boffi, F. Brezzi, L.F. Demkowicz, R.G. Durán, R.S. Falk, M. Fortin, Mixed Finite Elements, Compatibilty Conditions, and Applications, in: Lecture Notes in Mathematics, vol. 1939, Springer, 2008.
[36] M. Ainsworth, J.T. Oden, A Posteriori Error Estimation in Finite Element Analysis, Wiley, New York, 2000.
[37] M. Reynier, P. Ladeveze, N.M.M. Maia, Error on the constitutive relation in dynamics, in: H.D. Bui, M. Tanaka, et al. (Eds.), Inverse Problems in Engineering, Rotterdam, Balkema, 1994, pp. 251–256.
[38] P. Wriggers, Nonlinear Finite Element Methods, Springer-Verlag, Berlin, 2008.